TASK QUARTERLY 2 No 3 (1998), 385–415

DISCRETE ELEMENT MODELLING OF INDUSTRIAL GRANULAR FLOW APPLICATIONS

PAUL CLEARY

CSIRO Division of Mathematical and Information Sciences
Private Bag 10, Clayton South MDC, Clayton, Vic, 3169, Australia

Abstract: Discrete element methods for modelling granular flows have now developed sufficiently for them to be applied to complex industrial and mining applications with an expectation that they can predict these flows reasonably well. Furthermore detailed quantitative predictions can be made using these models, allowing them to be validated against carefully designed experiments and then iteratively improved. The models allow existing equipment and processes to be carefully analysed. The resulting enhanced understanding can then be used to help improve them or to create new ones. DEM modelling of a wide range of industrial applications are described in this paper, including ball mill operation, dragline bucket filling, vibrational segregation by size and density, flow in centrifugal mills, flows from slot hoppers, idler induced segregation, cutter bias for commodity samplers and mixing in tumblers.

1. Introduction

Particle flows occur in a broad spectrum of industrial and mining applications. These range from separation and mixing (such as in making glass and pharmaceuticals), to grinding and crushing, blasting, rotary moulding (such as of plastics), commodity sampling, stockpile construction, open cut mining, excavation, generic flows in and from hoppers, silos, bins, conveyor belts and many more.

Discrete element modelling (DEM) of granular flows involves following the trajectories, spins and orientations of all the particles and predicting their interactions with other particles and with their environment. These methods are now well established and are described in review articles by Campbell [1], Barker [2] and Walton [3]. DEM has used been successfully used for over a decade in modelling geophysical applications, such as landslides [4, 5] and ice flows [6].

Many industrial applications are more demanding since it is necessary to simulate particles of wider size and density ranges (in order to capture the effects of interest) interacting with often complex shaped objects moving in a range of different ways. The key ingredients are a fast and robust algorithm to predict collisions, an adequate contact force/collision model and an efficient and powerful way to describe the boundary objects.

Much of the existing industrial DEM modelling involves studies of either ball mills (first performed by Mishra and Rajamani [7]) and hoppers, bins or silos (which

have been studied by many of authors). A recent report [10] compares more than thirty eight DEM calculations of the filling of a standard silo. A surprising amount of variation was found for what is essentially a simple and standard underlying algorithm. The variation seems to lie in the implementation details of the models and the choice of the contact force.

DEM simulations of a much wider range of industrial applications have been performed by this author [11, 12, 13, 14, 15, 16, 17] and are summarised in this paper. These include ball mill operation, dragline bucket filling, size and density segregation due to shaking, hopper flows, charge motion in centrifugal ball mills, particle microstructure in stockpiles, idler induced segregation on conveyor belts, commodity sampling by cutters and mixing in tumbling containers.

Visualisation of industrial granular flows plays an important part in understanding these complex flows. However, the detailed information available in DEM simulations also allows a wide range of relevant quantitative predictions to be made, including estimates of wear rates and distributions, collisional force distributions, dynamic loads on boundaries, power consumption, torques and flow rates. Mixing and separation rates can also be calculated. Such tools, once validated, allow existing equipment and processes to be analysed in detail and the enhanced understanding can then be used to help improve them or to create new ones.

2. The Discrete Element Simulation Method

In discrete element simulations each individual particle is modelled and all their collisional interactions with each other and with their environment are modelled. Equations of motion are solved for the boundary objects with which the particles interact. For industrial applications it is important to be able to model boundary objects with complex geometries. This requires a powerful, flexible and convenient way of describing them. In our two dimensional code, objects are constructed from segments which can be lines, circular segments or discs. Nearly arbitrary shaped two dimensional boundary objects can then be constructed. Arbitrary rigid body and surface motions can also be specified. External forces, such as cables for supporting dragline buckets, can be attached to objects.

Our particles are modelled as either discs or super-quadrics whose general form:

$$x^n + \left(\frac{y}{A}\right)^n = s^n , \tag{1}$$

is used to describe non-circular particles, where the power n determines the sharpness or blockiness of the particle (with the shape smoothly changing from a circle to a square as n increases) and A is the aspect ratio of the particle with semi-major axis s, (note that this is not the radius of the particle). Aspect ratios of up to 10:1 and sharpnesses of up to 20 can be used. These shapes are able to capture many of the essential elements of real particle shape and greatly extend the range of applicability of the DEM.

The particles are set up as groups with any number of independent groups of particles specifiable. Each can be made from multiple independent subgroups, whose

diameters, densities, aspect ratios, sharpnesses and material properties can be independently specified according to selected probability distributions. Generally these are constant, uniformly distributed or normally distributed, but other more specialised ones such as Ross and Rambler can be used. Packed particle microstructures are built by filling user-specified polygons with these particles. The simulation code takes these input data, generated by a graphical pre-processor and performs the required simulation collecting output data that is appropriate for the application.

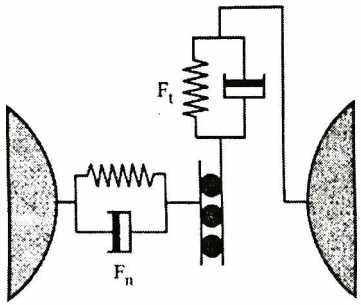

Δx is the particle overlap,
k_n and k_t are the normal and tangential spring constants,
v_n and v_t are the normal and tangential velocities,
C_n and C_t are the normal and tangential damping coeffs
μ is the friction coefficient

Normal Force $F_n = -k_n \Delta x + C_n v_n$

Tangential Force $F_t = \min(\mu F_n , k_t \int v_t dt + C_t v_t)$

Figure 1. *The contact force model involves a spring and a dashpot in the normal direction and an incrementing spring and dashpot limited by the sliding friction in the tangential direction.*

The DEM variant used here is sometimes called a "soft particle method". The particles are allowed to overlap and the amount of overlap Δx, and normal υ_n and tangential υ_t relative velocities determine the collisional forces. There are a range of possible contact force models available that approximate the collision dynamics to various extents. A conventional linear spring-dashpot model is used in these simulations. Other more complex forms are available (see Schafer *et al.* (1996) and Walton (1994) for details). Figure 1 shows diagramatically the collisional force model used here. The normal force:

$$F_n = -k_n \Delta x + C_n v_n \,, \tag{2}$$

consists of a spring to provide the repulsive force and a dashpot to dissipate a proportion of the relative kinetic energy. The maximum overlap between particles is determined by the stiffness k of the spring in the normal direction. Typically average overlaps of 0.1–1.0% are desirable, requiring spring constants of the order of 10^6–10^7 N/m. The normal damping coefficient C_n is chosen to give a required coefficient of restitution ε (defined as the ratio of the post-collisional to pre-collisional normal component of the relative velocity):

$$C_n = 2\gamma \sqrt{m_{ij} k_n}$$

where

$$\gamma = -\frac{\ln(\varepsilon)}{\sqrt{\pi^2 + \ln^2(\varepsilon)}}, \qquad \text{and} \qquad m_{ij} = \frac{m_i m_j}{m_i + m_j}$$

is the reduced mass of particles i and j with masses m_i and m_j respectively. This arises from the analytic solution of the normal collision equation (2) for two such particles. Each particle can have a different coefficient of restitution (and corresponding damping constant), but we generally use the same value for all the particles because of a lack of data required to describe the variations in ε.

The tangential force is given by:

$$F_t = \min\left\{\mu F_n, k_t \int v_t dt + C_t v_t\right\}, \tag{3}$$

where the integral of the tangential velocity v_t over the collision behaves as an incremental spring that stores energy from the relative tangential motions and represents the elastic tangential deformation of the contacting surfaces. The dashpot dissipates energy from the tangential motion and models the tangential plastic deformation of the contact. The total tangential force (given by the sum of the elastic and plastic components) is limited by the Coulomb frictional limit at which point the surface contact shears and the particles begin to slide over each other.

The contact force model requires both the coefficient of elasticity and friction for the particles to be supplied. Such quantities are in practice very difficult to obtain experimentally and can vary strongly between particles of the same material. This partially follows from the variability of real materials and because these model paramaters are not themselves really true reflections of reality, but are highly idealised. The development of better contact force models that reflect this and whose parameters can be measured robustly is an important element of further improving the predictive power of discrete element modelling.

The discrete element algorithm itself is relatively simple with three essential parts:

- A search grid is used to periodically build a particle near-neighbour interaction list. The boundary objects appear as virtual particles. Details of the search algorithm can be found in [19]. Using only particle pairs in the near neighbour list reduces the force calculation to an $O(N)$ operation, where N is the total number of particles. Some mechanism such as this is essential for using realistic numbers of particles (presently up to 80.000).
- The collisional forces on each of the particles and boundary objects are evaluated efficiently using the near-neighbour list and the spring-dashpot interaction model (shown in Figure 1) and then transformed into the simulation frame of reference.
- All the forces on the objects and particles are summed and the resulting equations of motion are integrated:

$$\dot{x}_i = u_i, \qquad \dot{u}_i = \sum_j F_{ij} + g \tag{4}$$

$$\dot{\theta}_i = \omega_i, \qquad \dot{\omega}_i = \sum_j M_{ij}, \tag{5}$$

where x_i, u_i and F_{ij} are the position, velocity and collisional forces on particle i, and θ and ω_i are the particle orientation and spin produced by the moments M_{ij}. Here g is the gravity vector.

The integration scheme is a second order predictor-corrector. Between 20 and 50 timesteps are required to accurately integrate each collision, leading to very small timesteps (typically 10^{-3} to 10^{-6} s depending on the controlling length and time scales of each application). If the integration is accurate then the coefficient of restitution from which the damping coefficient was chosen should be recovered. A higher order integration scheme using a larger timestep may seem attractive, but the timestep is also constrained by the requirement that for two particles moving together the initial overlap is at the very worst a couple of percent. In some cases, this is a more stringent constraint on the timestep than the earlier one and eliminates any advantages of the higher order scheme. Overall the explicit integration timestep is given by:

$$\Delta t = \min\left(\frac{\pi}{25}\sqrt{k/m_{ij}\left(1-\gamma^2\right)},\ 0.1\ d_{min}/n_s U_{max}\right)$$

where U_{max} is the maximum particle velocity, d_{min} is the smallest particle diameter and n_s is the number of timesteps between searches.

3. Data collection and quantitative predictions

Granular flows can be analysed with visualisation and data processing tools to provide quantitative predictions about wear rates and distributions, collision forces, dynamic loads on boundaries, power consumption, torques and flow rates, sampling statistics, mixing and segregation rates. This requires the disordered particle data to be collected in bins, possibly smoothed and then displayed in an informative way.

3.1 Bins and smoothing

In such DEM simulations, the positions, velocities, orientations and spins of all the particles and the collisional forces are known at all times. The estimation of variables from disordered data requires the data to be collected into bins. This is a difficult task for an general object oriented package where the binning strategy must work for all complex objects. Such a system has been implemented for our code.

Two types of data are collected:

- One dimensional data along the surfaces of objects. This includes normal, tangential and total boundary forces. This allows prediction of wear rates, wear distributions and dynamic particle pressures on boundaries. The surfaces of each object are subdivided into sequences of equal sized bins. Each object segment can have its own sequence of bins or a sequence can follow the edges of several segments depending on needs. Information about each collision is stored in the appropriate bin. Figure 2 shows a typical set of bins for part of the liner of a ball mill.

Two dimensional data about forces, average velocities and spin, velocity correlations (equivalent to Reynolds stresses) and granular temperature within the flowing granular material. These can be used for a range of purposes including estimation of the grinding efficiency of comminution devices. The desired rectangular region is subdivided into square bins that move and rotate with the specified reference object.

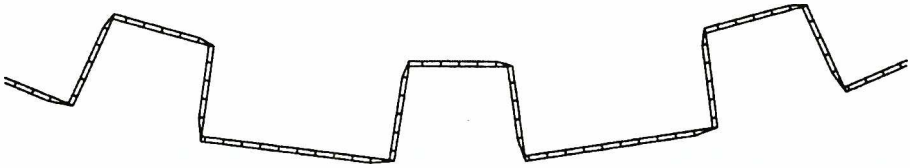

Figure 2. *The bin sequences for data collection around the lifter bars in a ball mill.*

A major problem with any form of binned data from discrete element simulations is its tendency to be very spiky. Figure 3a shows the spikiness of the force distribution under a small pile of particles. This arises principally from the discrete nature of the particles.

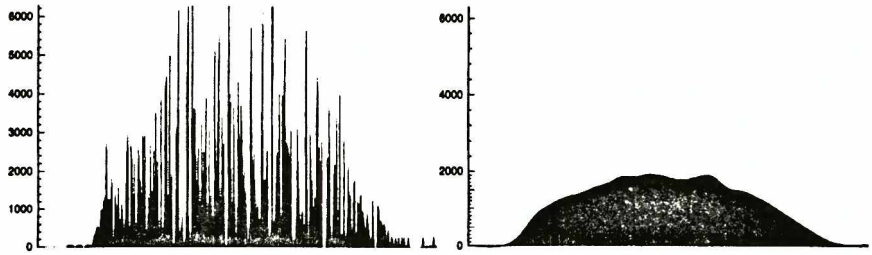

Figure 3. *The pressure exerted on a horizontal surface by a rounded pile of particles (a) the unsmoothed force data and (b) the smoothed estimate of the boundary pressure.*

The spikes can be removed by appropriate smoothing. Most industrial applications are quasi-steady for only short time periods, so only short period time averaging is possible and more sophisticated spatial smoothing is required. We use a Demmler-Reinsh formulation of cubic spline smoothing algorithm [14]. The amount of smoothing is controlled by a smoothing parameter, which determines the balance between exact curve fitting and the smoothing. The smallest meaningful scale on which data can be gathered is determined by the smallest particle size d_{min}, so we choose the bin size to be $d_{min}/2$. The length scale of the spikiness is determined by the size of the largest particle d_{max}. The smoothing parameter is chosen to remove more than 90% of variation whose length scales are less than d_{max}. Smoothing is applied independently to each bin sequence, since it is not appropriate to smooth data around sharp corners. Details of the binning and smoothing can be found in Cleary [15].

3.2 Measuring mixing or segregation

Flowing granular materials undergo both mixing and segregation in industrial processes ranging from minerals and food to pharmaceuticals and ceramics. Sometimes it is desirable to enhance the mixing and inhibit segregation and in other cases it is desirable to minimise the mixing and enhance the segregation. The distribution of local averages of the particle size, mass or density characterises the spatial variation of the particle composition from the average. The amount of mixing or separation for granular materials can be measured by the coefficient of variation of this distribution. Comparing this to the values occurring for perfectly mixed and perfectly segregated materials allows the mixing state to be described by a single number in the range of 0 to 1. Its time variation then quantifies the mixing or segregation rates. One significant advantage of such an approach is that it does not rely on trying to correlate the mixing state with any particular spatial dimension and is therefore very general in its range of application. More details of this method and examples are given in [16].

3.3 Wear predictions

Wear predictions can be made from the collision data collected in the object bins using the Finnie model [20, 21]. This uses particle impact speeds and material hardnesses to estimate the wear produced by each impact. The Finnie model contains a parameter c which is the fraction of particles cutting in an idealised manner. On average this is the proportion of kinetic energy that goes into producing wear. This value needs to be determined experimentally for each application and is unknown in this case. Our best estimate found by comparing anecdotal wear rates with our predictions for dragline buckets and ball mill lifters is around 0.1 to 0.2.

4. Ball mill

Ball mills are large rotating drums (up to around 5 m in diameter) used for grinding rock in the mineral processing and quarrying industries. The rock generally comes from a crusher or perhaps a semi-autogenous (SAG) mill (depending on the design of the milling circuit) and is feed into one end of mill. Grinding media consisting of steel balls with sizes in the range 5 to 20 cm is already present in the mill along with rock that is still to large to pass out through the extraction grate at the opposite end. Particles migrate slowly along the length of the mill while circulating rapidly with the mill shell in the plane orthogonal to the mill axis. The radial and azimuthal particle motion is assisted by lifter bars attached to the mill shell. Replacable liner plates are bolted to the shell between the lifters to reduce wear in this hostile environment.

A typical 5 m diameter ball mill consumes around 3 to 4 MW of power and has energy efficiencies of around only 1 to 5%. Significant economic and environmental benefits can be obtained by improving this efficiency even modestly. There are also significant costs involved in replacing the liners (commonly made from expensive wear resistant cast molybdenum stainless steels) arising both from the liner

replacement cost and from lost production. Further significant benefits can be obtained through higher downstream recovery if the exit particle size distributions can be made closer to the optimum for the subsequent flotation processes.

Simulation of ball, SAG, AG, pebble, tower and many other types of mills by discrete element methods offers enormous prospects for improving the efficiency and productivity of comminution processes. In this section we report a summary of some of our DEM results for ball mills. This builds on earlier work by Mishra and Rajamani [7, 8, 9]. Ball mills are one of the more difficult applications to model because of the scale of the mill, the huge numbers of particles that are present in the mill, the presence of water (which we currently neglect) and the timescales involved in the comminution processes. Directly modelling the actual particle size reduction by attrition and breakage is an even greater challenge.

In this paper we concentrate on the behaviour and performance of a 5 m diameter ball mill with 23 symmetrically placed lifter bars rotating clockwise at various fractions N of the critical speed of 19.5 rpm at which an average size ball

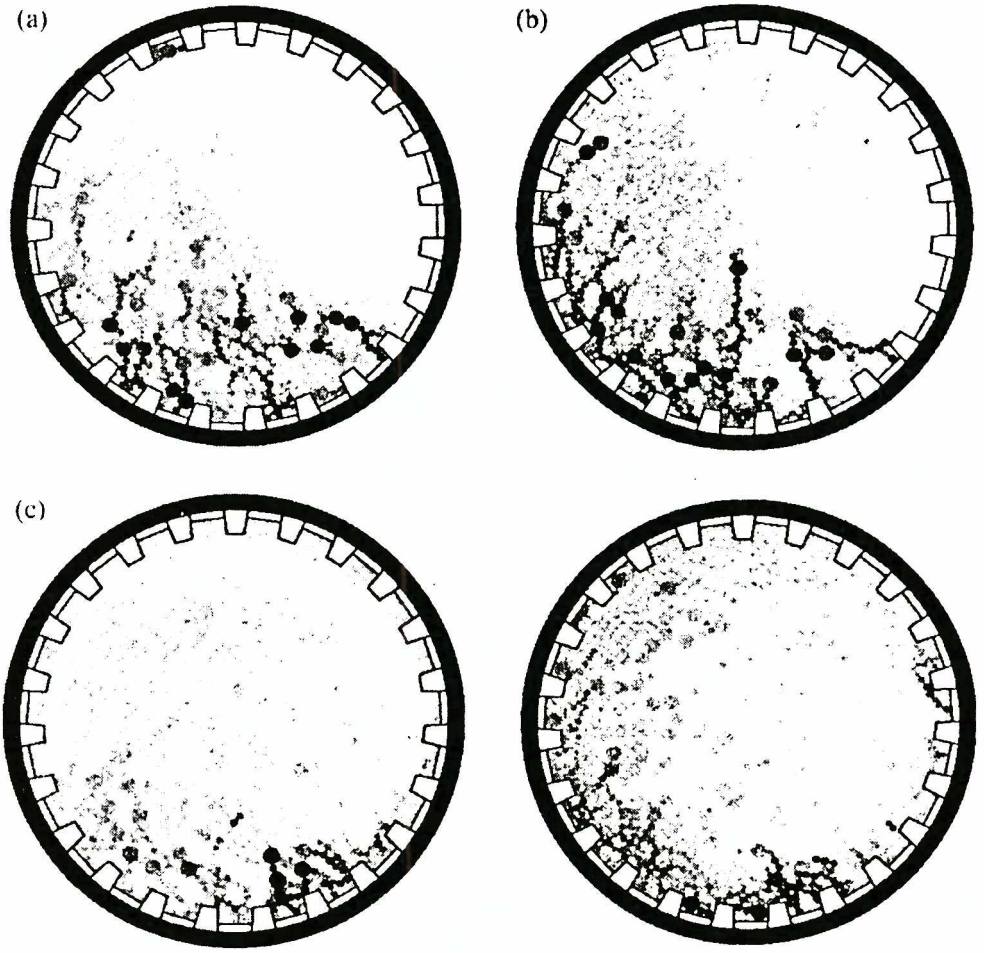

Figure 4. Charge motion for a) N = 60%, b) N = 80%, c) N = 100% and d) N = 120%.

begins to centrifuge. The solids loading used throughout is 50%. This ball mill rotates with constant speed. The torque required and energy consumption of the mill can then be predicted. Alternatively a constant torque could be applied and the subsequent motion predicted. The effects of the inertia of the mill itself can also be included.

To begin, we consider a charge that consists only of the steel balls with 5% by number of 200 mm diameter and equal numbers of 100 and 75 mm particles. They have a coefficient of restitution of $\varepsilon = 0.3$ and friction of $\mu = 0.75$. The location of the charge in the mill is shown in Figure 4 for various mills speed. For $N = 60\%$ the bulk of the charge lies in the lower left half of the mill and its motion is relatively gentle. Balls rotate from the toe position (at about 4 o'clock) up to the shoulder around 10 o'clock. The charge fluidises and cascades down along the free surface to the toe. There is very little cataracting (ballistic) material.

For $N = 80\%$, (Figure 4) much of the charge fluidises above the center of the mill and the free surface develops the bi-linear shape characteristic of high rotation rate mills. A moderate amount of cataracting material now impacts on the liner to the right and on the charge in the toe region. For $N = 100\%$, (Figure 4c) particles begin to centrifuge and can be seen trapped between the lifters. Much of the core of the charge is now cataracting. Mills are generally run sub-critical ($N < 100\%$) because little grinding can be achieved with the centrifuged material and significant lifter wear is produced by the cataracting material. For $N > 120\%$ the thickness of the centrifuged layer exceeds the height of the lifters.

The comminution is produced by at least three different mechanisms

- *Breakage by high energy normal collisions*: These occur when large cataracting rocks or the steel balls impact at high speed on either the toe region or the liner. Rock impacts with the liner produce useful breakage and liner wear. Ball impact with the liner damages both the balls and the liner and is very undesirable. The position of the toe varies with fill level (which in turn varies with the hardness of the rock, the mill rotation rate, the water flow rate and the feed rate) and is generally not known. Significant work continues to determine where the charge is and how to control it. The crushing produced by the balls falling onto the rocks in the toe has been the focus of much of the modelling and experimental mill work.

- *Attrition*: The shearing action in both the avalanching region and near the shell in the region where material is being lifted produces attrition where very small fragments are ripped/rubbed from the larger ones which become progressively more rounded. This is a very important mechanism once the breakage mechanism has exhausted the major flaws in the larger rocks and reduced them to below 50–100 mm.

- *Low energy crushing near the shell*: In a granular material most of the force is transmitted via a small number of chains of particles, the members of which experience very large instantaneous forces. The particles in Figure 4 are shaded according to the instantaneous total collisional force (with black showing the highest

level) and show these chains in the bulk of the charge very clearly. They are generally curved and end at the liner in the lower part of the mill. The intensity of the forces increases with depth into the charge. These chains change extremely rapidly as the microstructure continuously adjusts to small changes in the mill orientation. Very high instantaneous forces are experienced by only small number of particles in these chains at any given time. If these forces produce tensile forces within the particles that exceed their yield stresses then they are crushed. This is a very low energy but high force crushing mechanism for the larger particles and contrasts to the first high energy mechanism.

Modelling the actual size reduction in a full scale mill by DEM would involve tracking particles with sizes less than 100 microns. The length scales and numbers of particles are presently prohibitive. We therefore use the DEM to calculate quantities such as the rate of particle-particle and particle-wall shear and normal work and use these as indicators of the breakage and the attrition. This allows comparison of comminution performance for different mill configurations.

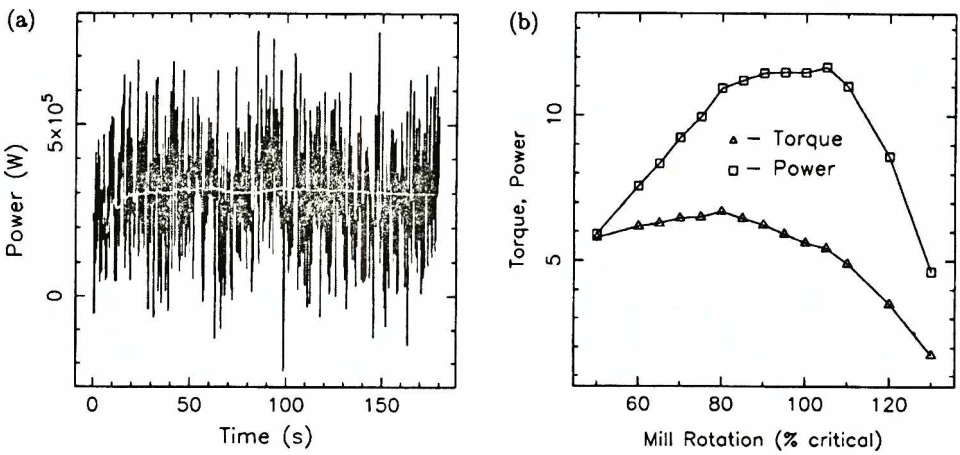

Figure 5. *Power draw for N=80% and b) average torque and power for several speeds.*

The torque required to maintain a constant speed and the power consumption of the mill can be predicted. Figure 5c shows the instantaneous power draw of the mill shown in Figure 4 for three minutes of operation at $N = 80\%$. The running average of the power is shown by the grey line. The average power is 3×10^5 W per meter of mill length. This gives a total power draw for a typical 7 m mill of 2.1 MW. This compares well with a typical motor power of 3.3 MW. Superimposed on this average power draw are irregular high frequency fluctuations of 130% of the mean reflecting the highly impulsive and unsteady flow of the charge. Figure 5b shows the variation of the torque and power with mill speed. The torque increases slowly until the peak is attained for $N = 80\%$. As the amount of cataracting and then centrifuging increases, the balance of the charge improves and the torque required

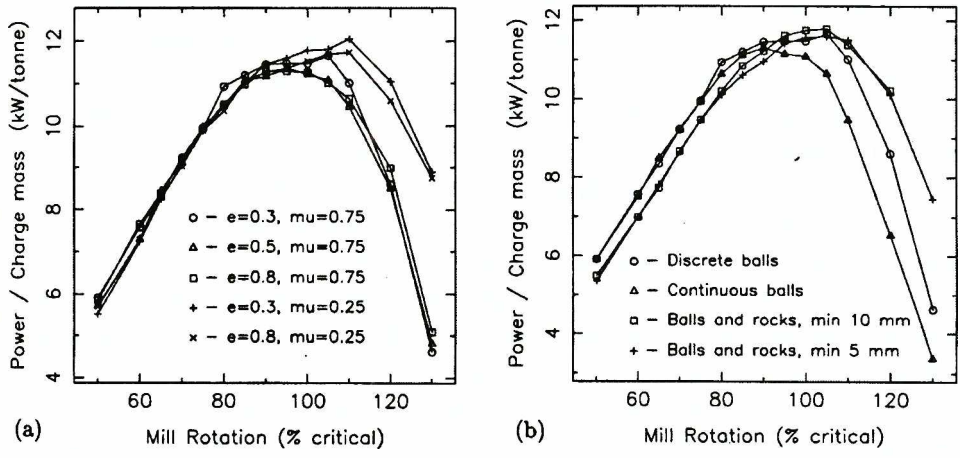

Figure 6. *a) power draw for 50% fill for different values of ε and μ , b) power draw for 50% fill with different particle size distributions.*

to maintain the asymmetric charge position drops steadily. The power (the product of the torque and the mill speed) consequently has a much rounder peak centered on $N = 90\%$ before dropping sharply above 110%.

The material parameters ε and μ and particle size distribution for the rock vary between mines and within mines and are also likely to be modified by the presence of water in the mill. It is therefore important to understand the effect of variability in the material parameters on the mill performance. Figure 6 shows the power draw versus mill speed for a range of material properties and particle sizes. The base case with $\varepsilon = 0.3$ and $\mu = 0.75$ is shown by the circles and is the one shown in the previous figure. Increasing the coefficient of restitution to 0.5 has only a modest effect on the power draw curve. At low speeds $N \leq 75\%$ there is little change at all. For the intermediate speeds (in which the mills are most commonly operated) and high speeds there is a reduction in power consumption of between 2 and 6%. Increasing ε to 0.8 has a much smaller effect on the power draw.

Reducing the friction coefficient to 0.25 (due to the lubricating effects of the interstitial fluid), we find only a small change in the power draw below 75% critical speed. One may expect a large decrease in the friction may have significantly increased the power draw, but this change does not affect the dynamics of the much of the charge motion. The bulk of the charge is actually locked together and rigidly rotating. The material outside the avalanching region near the surface of the charge is not sliding, so the energy consumption is not affected by the lower limit on the sliding friction. In the avalanching layer the lower friction does reduce the power consumption, but these particles are a minority of those in the charge and the particle contacts are generally not long duration sliding ones. This leads to only a small reduction in the energy consumption. At higher sub-critical speeds and the super-critical speeds the power consumption actually rises with the lower friction. This is counter-intuitive but can be explained by the lower friction increasing the

mobility of particles, particularly in the centrifged layer at high speeds. These more mobile particles lead to a more unbalanced load and higher dissipation rates due to the normal collisions. At $N = 130\%$ the power draw is actually doubled.

Figure 6b shows the variation of the power draw curves with changes in the particle size distribution. The circles show the power draw curve for the original particles used in Figure 4. Changing the particle size distribution from these three discrete sizes to a continuous uniform distribution between 50 and 200 mm gives the power draw curve given by the triangles. For $N \leq 75\%$ there is negigible change in the power draw. For higher sub-critical speeds the power draw is reduced by 2 to 5% for the continuous size particles. For super-critical speeds there is a significant reduction in power consumption of 20–25%.

Using the same continuous ball distribution and adding rocks with sizes uniformly distributed between 10 and 50 mm (with ten times more rocks than balls) we obtain the power draw curve given by the squares. This is consistently around 0.5 kW/tonne lower than for the balls alone for speeds below 80%. This is an decrease of 5 to 8% and occurs in the speed range which previously has been quite insensitive to changes. At higher speeds the difference between the power draw for the ball and rock case and the pure ball case declines. The ball and rocks have a higher power draw for $N > 95\%$. For speeds up to 105% the ball and rock case then has a higher power draw by around 2%. For higher speeds this case has a significantly higher power draw. Note that the overall shapes of the power draw curves are similar and that the peak power occurs at around the same speed.

Decreasing the bottom size of the rocks to 5 mm gives the power draw curve shown by the plus markers. For low and high speeds the power draw is very similar to the previous case with the 10 mm bottom size (squares). However, in the region $80 \geq N \geq 105\%$ the power draw for the case with the smaller bottom size is reduced by around 2%. It is not clear why the charge motion and power should be mildly sensitive to the choice of bottom size in this region. The necessity for the particle size distribution to be truncated (in order to keep the size of the DEM simulations

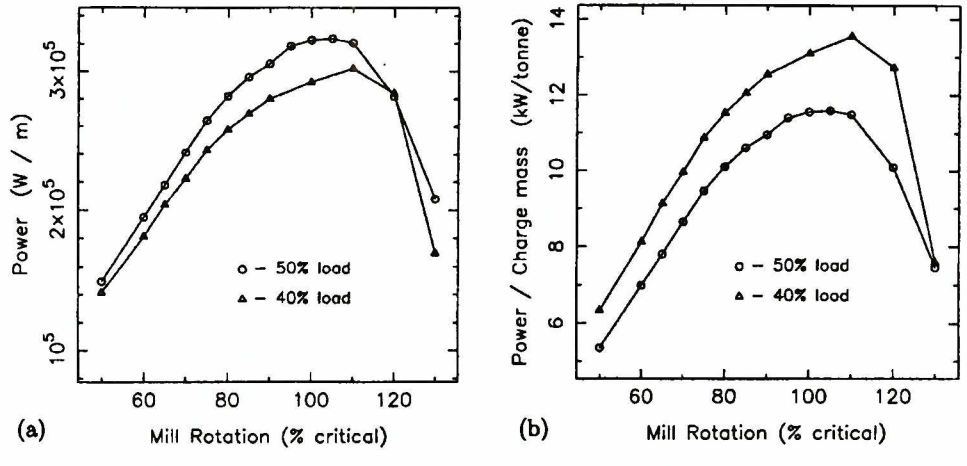

Figure 7. a) Power draw and b) power consumption/tonne, for 40% and 50% fill levels

feasible) and overlap of this sensitive region with the most commonly used operating speeds, indicates that some care needs to be made in extrapolating DEM to real mills. These truncation size effects could be responsible for errors in the prediction of the power draw of a few percent. The variation of the power draw by several percent with particle size distribution also reflects the well known sensitivity of real mill performance to changes in the feed composition.

Overall these sensitivity analyses indicate that a mill operating at or below 75% critical is insensitive to the changes in material properties of the charge but is sensitive to changes in the size distribution. This means that mills operated at these speeds should be more stable in their operation and easier to control than the same mill operating at higher speeds. Variations of 2–6% are observed with variations in the material properties for higher rotation rates. At higher speeds, lower friction material actually leads to higher power draw. This appears to be particularly important for mills that are operated super-critical.

Figure 7a shows the power draw as a function of mill speed for the original 50% and also for the 40% fill level using a charge consisting of both balls and rocks with a bottom size of 5 mm. As expected the smaller charge consumes less power, except at N=120% where the power is equal. At 130% critical there is a significant drop in the power draw, since for this lower fill level almost all the particles are being centrifuged. Interestingly, the peak of the power draw has moved from around $N = 95\%$ for the 50% fill level to 105% for the 40% fill level. This is the first occasion that any change in the mill configuration or particles has altered the location of the peak power consumption.

The power consumption per tonne (or power density) is more interesting and is shown in Figure 7b. It is considerably higher for the 40% fill level, by between 15 and 20%. The rate of particle grinding is actually dependent on the local rate of energy dissipation or power density rather than on the total power consumed. This figure shows that better grinding will occur with a lower total energy consumption for a 40% full mill rather than one jammed to near or above capacity at 50%. This clearly illustrates the well known observation that an overfilled mill suffers from reduced grinding efficiency. Shortly we will identify the optimum fill level for this mill and set of particles. It is expected to be around 30–35%.

The particles used so far have all been circular. Figure 8 shows a snapshot of the balls (using the original discrete size distribution) at a rotation rate of $N = 80\%$ for both circular and non-circular particles. The non-circular particles have aspect rations between 0.5 and 1 and sharpnesses from 2 to 5. This give particles that vary between circular and elongated blocks. The flows are qualitatively very similar, with the shape and angle of the free surface being very similar and similar amounts of cataracting material.

There are however, some key differences. The particles in the upper half of the charge are flowing down the free surface. Any flowing non-circular material behaves quite differently because this material is forced to dilate in order for the spinning particles to pass each other. This produces a noticeably higher void fraction

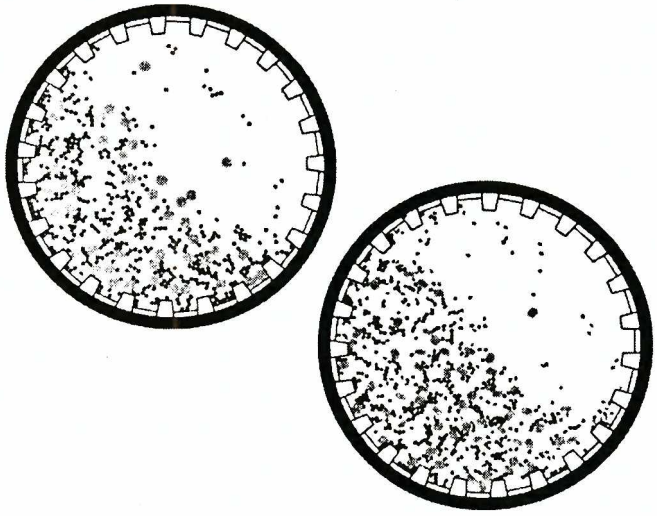

Figure 8. *a) Mill with circular particles and b) mill with non-circular particles.*

in this upper flowing region. The expansion of this region lifts the free surface higher, which in turn raises the height of the cataracting stream. All three of these differences are clearly visible in this figure. The non-circularity of the particles also increases the shear strength of the non-flowing material in the lower half of the charge. It is not clear whether this has affected the location of the central shear zone, but any effects of increased microstructural strength appear at best to be small. Interestingly, the power density for these circular and matching non-circular particles are within a couple of percent of each other. This suggests that the changes produced in the mill performance by non-circular particles are quite small and that the results obtained using circular particles both here and by other authors may be closer to reality than may have been thought possible.

Other quantitative predictions can also be made. Figure 9a shows the intensity of the collisions within the ball mill for the first particle set. The collisional intensities in the bulk of the charge increase with proximity to the bottom, reflecting the

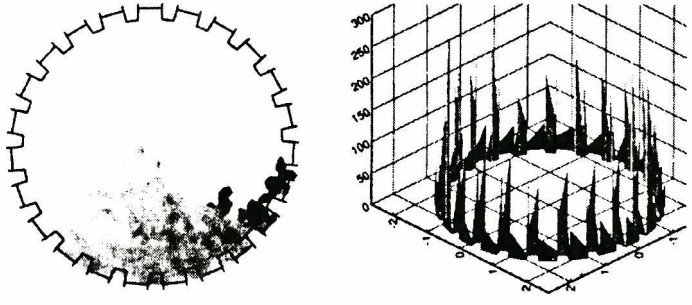

Figure 9. *(a) Collision intensity within the ball mill and (b) wear on the liner of the ball mill*

increasing weight of material above. The collisional forces are slightly higher in the surface avalanching region. The forces are higher at the base of the avalanches where additional force must be applied to halt the downward flow of this material. The high intensity region in the lower right is caused by impacts of the cataracting material on the liner and on the tail of the charge. Predictions of attrition and breakage rates can be inferred from such collisional force data.

Figure 9b shows the wear predictions for this particular ball mill. The wear pattern on the lifter bars is reasonably regular and is concentrated on the top and front surfaces of the lifter bars with the highest wear at the corners. The wear on the front surface decreases with the distance from the leading edge. The wear on the top surface increases with distance from the leading edge. The wear on the back of the lifters and between them is much smaller. On the back face it decreases with distance from the top of the lifter bar. The wear between the lifters is largest at the back of a lifter bar and decreases as the next lifter bar is approached. Using a wear efficiency parameter of 0.1 gives a peak wear rate of around 25 mm/1000 hours of ball mill operation. This is broadly consistent with observed erosion rates, although accurate experimental figures are very difficult to obtain.

5. Charge motion in centrifugal mills with various loadings

A 30 cm centrifugal mill, used for high intensity and ultra fine grinding, is shown in Figure refcmill for different particle loadings. The cylinder executes a centrifugal motion with diameter 12 cm. The supporting arm rotates at 1000 rpm while the mill cylinder counter-rotates at the same rate. It is filled with uniform 6 mm particles and there are four flat lifters. These parameters were chosen to match the experimental configuration used by Hoyer [22].

Comparing these charge profiles with the high speed photographs of Hoyer we find very close agreement. Our 75% and 50% loaded cases did exhibit a steady stable charge profile that simply rotated with the mill whilst the granular material deformed smoothly. This is in accordance with the behaviour observed experimentally. Furthermore our charge profiles matched the experiments very closely, with the 75% case being indistinguishable even to the point of predicting the same amount between the lifter and the charge as the charge separate the lifter at the top.

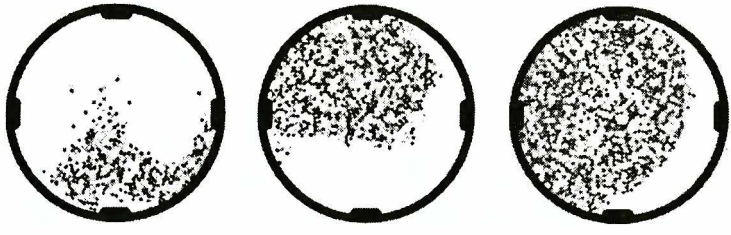

Figure 10. *Centrifugal mill charge profiles with loadings (a) 25%, (b) 50% and (c) 75%*

Theoretically there is a complete change in the flow behaviour for loads less than 30%. This also observed experimentally. Our simulation of the 25% loaded case exhibits the same unsteady flow as the experiments with the particles forming a characteristic distorted three pointed shape that flops around the the inside of the mill with a tumbling motion spraying loose particles all around.

This is one of the few applications for which we have been able to obtain high quality visualisation data. The very close agreement between the simulations, the experiments and with the theory gives us a degree of confidence that the DEM approach of trying to correctly model the applications at the particle level is capturing sufficient reality to give good predictions. One important caveat is that the particles used in the experiments were very close to spherical and so the circular particles used to model them are a good approximation. Cases where the real particles are really non-circular are not always well matched by DEM simulations using circular particles. Flows such as in hoppers and in slowly rotating tumblers where the material is partially stationary and then must shear can be significantly affected by ignoring particle shape.

6. Excavation by draglines

Draglines are huge earth moving machines used to remove overburden in open cut coal mining. A bucket (with capacity up to 100 m^3 and shown in Figure 11b) is lowered to the surface of the overburden and dragged back up the slope towards the machine. The teeth on the leading edge lift material into the bucket which is then emptied. A typical operation is shown in figure refdraglinea. The performance of these very expensive machines is affected by the bucket design, the mode of operation, the attachment of the cables (rigging) and the material properties of the overburden.

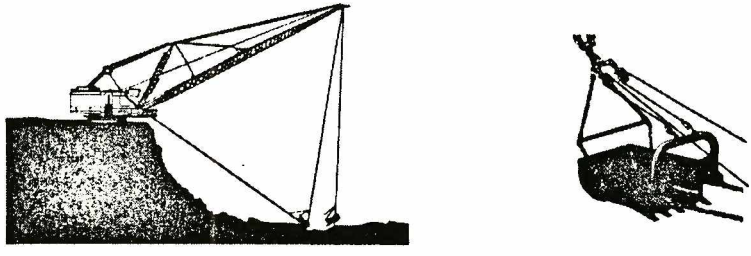

Figure 11. *(a) An operating dragline, (b) a bucket.*

Figure 12 shows the simulated filling of an Esco bucket. This 5 m long bucket is dragged up a slope of 22° with speed 1.75 ms^{-1}. The pre-blasted overburden is modelled as discs with diameters between 10 and 30 cm. The front lip lifts material which then surges up and into the bucket, stopping in layers. The flow involves a number of surges that relate to the amount and shear strength of the material in front of the bucket. Once the bucket has filled ($t = 6$ s) it is lifted by the supporting cables. By $t = 12$ s, the excess material has fallen off and the bucket disengaged from the ground. The filling time predicted is consistent with measured values. The

Figure 12. *An ESCO bucked filling with 10 to 30 cm particles, at t = 2 s, 5 s, 7 s and 9 s*

motions of the bucket are quite realistic as it is jolted around by the erratic nature of the particle collisions. The bucket angle constantly changes in response to the balance of forces applied.

The motion of the bucket was found to quite sensitive to the density and size distribution of the particles and to the attachment points of the cables. For a given material, incorrect rigging can cause the bucket to bury itself or to rise to the surface and skid along. These behaviours are consistent with the experience of dragline operators who believe that the material properties of the rock can strongly affect the performance of the dragline and the way it needs to be rigged.

Another bucket design known as the HP bucket is 5.5 m long and 1.6 m high, with a 0.25 m long lip that is inclined at 25º to the bottom of the bucket. This bucket is filled in the same way as the previous bucket with the same 10-30 cm particles. Again the rigging was chosen to give relatively stable bucket motion. Figure 13 shows this filling process. The initial material enters as a thin rolling layer (frame a) and continues up the back with some material falling out. The following material is

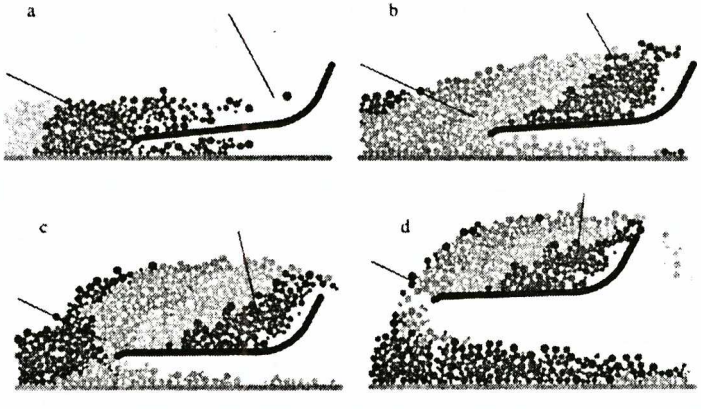

Figure 13. *A HP bucket filling with 10 to 30 cm particles at a) t=2 s, b) t=5 s, c) t=7 s and d) t=9 s*

slowed by collisions and stops before reaching the top, so that only a small amount of material falls out for a short time. There is little sign of the modest surges in the flow into the ESCO bucket. The much shallower lip acts only to separate the incoming material into two streams and does not impart much upward motion to the stream entering the bucket.

The lower back of the bucket means that the level to which the spoil rises before flowing out is lower. This is partially compensated for by the greater bucket length. The filling is otherwise broadly similar to that of the ESCO bucket. Some other small differences exist. The lower trajectory of the material entering means that the material already in the bucket is sheared more strongly at lower levels of the bucket. This produces an interface between the second band of material (dark grey) and the third (mid grey) that is essentially straight rather than convex.

The curved back of the ESCO bucket allowed the nearby particles to be slowly pushed upwards as they slide slightly along the back. The combination of the straight and curved sections of the back of the HP bucket lock the particles more tightly and prevents them from sliding upwards in response to the pressure generated by the particles being bulldozed in front of the bucket.

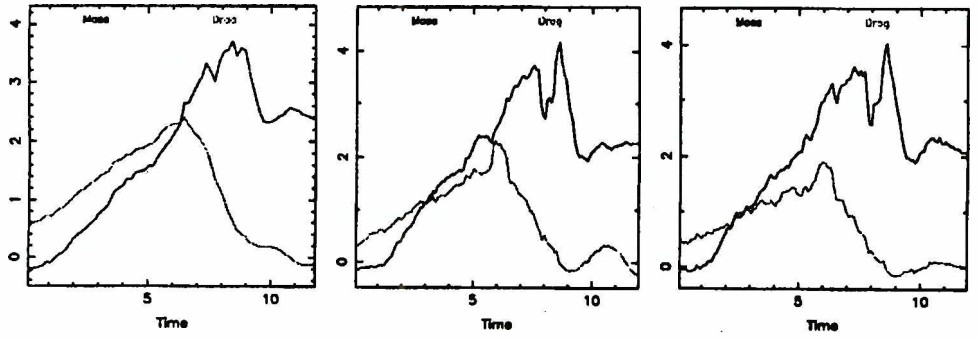

Figure 14. Drag coefficient and normalised mass of material contained in the bucket for: a) ESCO bucket with 10 to 30 cm particles, (b) ESCO bucket with mon-sized 20 cm particles, (c) HP bucket with 10 to 30 cm particles

The mass of material in the bucket and the particle drag on the bucket can be calculated from the cable tensions at all times. Figure 14 shows the drag (lower curve/ black) and mass of material in the bucket (higher curve/grey) for the three cases shown above. They are normalised by the weight of each bucket (about 10 tonnes/m). The three cases show qualitatively similar behaviour. The drag and mass increase linearly with time during the filling phase. After $t = 6$ s, when the lifting begins, the drag declines linearly as less and less material is pushed backwards by the rising bucket. The mass of material in the bucket continues to increase until around $t = 8$ s, as it becomes partially buried. After $t = 8$ s, material begins to flow off the top and the load declines, again linearly. The strong fluctuations in the curves around $t = 8$ and 9 s are caused by the impulsive starting and stopping of the bucket lifting.

The peak values of the drag occur around $t = 6$ s. Using the underlying linear growth behaviour (to exclude the effects of oscillations) the peak drags are

estimated to be about 1.9, 2.3 and 1.6 respectively for the three cases. The gradient of the drag curves provide useful estimates of the drag coefficients. For these cases the drag coefficients are 0.26, 0.29 and 0.17 respectively. By either measure the mono-sized particles clearly produce the highest drag and the HP bucket produces the lowest drag. The uniform particles in (b) are stacked in a hexagonal microstructure that resists breaking better and therefore exerts more drag on the bucket than the case with a large size distribution used in frame (a). The longer flatter HP bucket in (c) exerts a noticeably smaller drag than the taller Esco bucket in (a) when using the same particles. Conversely, the high back of the Esco bucket traps more material, (with a final spoil mass of $M = 2.25$), compared to $M = 2.05$ for the shallower HP bucket. The uniform size particles stack better and so produce the largest load at $M = 2.4$.

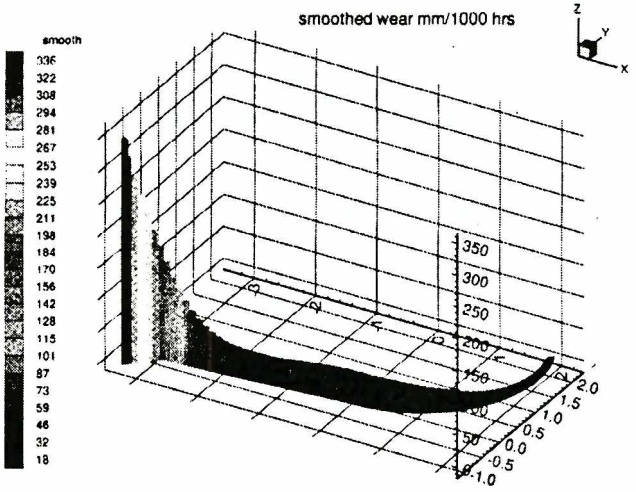

Figure 15. *Smoothed wear on the ESCO bucket after filling with 10 to 30 cm particles. To obtain real wear rates the ones shown here must be multiplied by a wear efficiency. A typical value of 0.1 leads to peak wear rates of 3 cm/1000 hours of continuous dragline operation at the tip of the cutting edge*

Figure 15 shows the smoothed wear predictions for the ESCO bucket using the particles with the 3:1 size range and a material hardness for toughened steel. The distribution is quite sensible. The peak wear occurs at the leading edge of the cutting teeth and declines steadily across the lip and the first meter of the bucket. This is caused by the large amounts of rapidly moving material that slides across these surfaces into the bucket. Once inside the particles move much more slowly and the wear is much lower and relatively constant, except for a broad low peak centered about 2.5 m from the back of the bucket. The particles are deflected upwards by the lip as they enter and the particles below do not support their entire weight, giving a lower normal force on the boundary than would occur if the particles were stationary. As gravity curves the trajectories down at about half-way into the bucket

the downward force exerted is slightly larger than the weight of the particles. The wear is dependent on how hard the particles are pressed into the boundary as they slide along it, leading to a modest increase in this region. The particles in the back of the bucket slide upwards very slowly leading to very low wear in this region. Overall, the wear distribution is sensible and consistent with the particle flow patterns.

The peak idealised wear predicted is about 340 mm of steel/1000 hours of operation. A reasonable guess for the wear efficiency parameter is around 0.1. This gives a peak wear rate of around 34 mm of steel/1000 hours, or about 3 cm every forty days. This is consistent with the best industry estimates that we have been able to obtain. Accurate data on wear rates for the teeth of dragline buckets is not available.

Bucket designs can be optimised using such simulations. Wear on the teeth and liners, the overall drag coefficient, the filling time and load capacity can all be predicted for alternative designs. Dynamic loads on the shell of the bucket can also be predicted and coupled with finite element analysis of the bucket to optimise its strength and weight. More information about this application can be found in Cleary [23].

7. Size and density separation by vibration

Separation of granular materials according to their physical properties is a very important process. Vibration induced segregation can be predicted by the DEM model. Figure 16 shows the initial state and state after 80 s of vibration of a box containing a binary mixture 8 cm particles (initially at the bottom) and 2 cm particles (initially on top). The initial hexagonal microstructure of the large particles is very stable making this a good test.

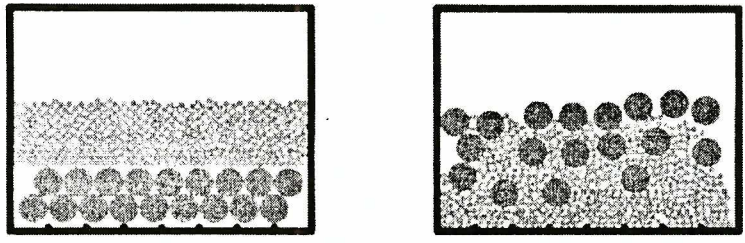

Figure 16. *Size segregation: Initial state and after 80 s shaking*

As the shaking occurs, short lived gaps are created in the microstructure, allowing small particles to fall to lower levels. The intrusion of smaller particles prevents the larger particles from returning to their previous packed state. This allows further small particles to fall into the now long lived gaps that been opened between the large ones. Eventually the small particles reach the bottom. In this example, the small particles behave as invaders, slowly eating away at the

microstructure of large particles. As each larger particle is separated it rises quickly to the surface. By $t = 80$ s the large particles clearly occupy the upper part demonstrating that size segregation can be predicted. Further segregation is prevented by the large scale convective motions generated by such vibration [24].

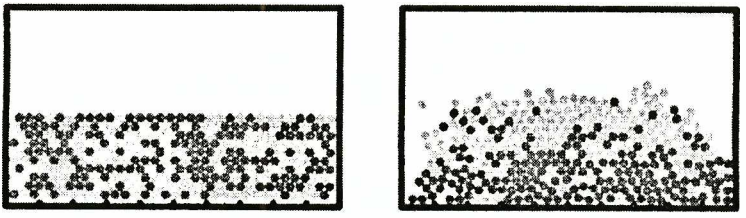

Figure 17. *Density segregation: Initial state and after 55 s shaking*

Figure 17 shows the initial and final state of a binary mixture of 3 cm particles. The lighter grey particles have density 1600 kg/m^3 and the dark grey ones are heavier have density 3600 kg/m^3. After 55 s of shaking, there is a clear concentration of heavy particles towards the bottom and lighter particles towards the top demonstrating that density segregation can be predicted by this model. The mechanism responsible for density segregation is presently not well understood.

Rates of segregation can be predicted using the methodology (described in section 3.2) involving the calculation of the coefficient of variation of the distribution of local average diameter or density. This allows optimal vibrational modes to be identified that give the best separation rates for given types of materials.

8. Idler Induced Segregation on Conveyor Belts

Material is often transported by conveyor belts, particularly in the mining and metal processing industries. These conveyors can be up to several kilometers in length and are supported by regularly spaced idlers. Between idlers, the belt has a catenary shape determined by the belt tension. The material on the belt is perturbed by the idlers which induce a slow but complex flow. We model a conveyor belt moving at 3 m/s with 10 cm diameter idlers spaced 3 m apart. The maximum belt deflection is 5 cm. This geometry is periodic and can be modelled with periodic boundary conditions in the flow direction. The progress of time is equivalent to following a group of particles moving along the belt. Figure 18 shows the particles at three times. These represent the state of the material at distances 6 m, 900 m and 4,050 m from the loading point. The particles are a binary mixture of 2.5 cm diameter and smaller 1.25 cm particles filling the belt to a depth of 20 cm. The particles are mixed randomly within this region.

The simulation plane is a slice through the center of the belt. As particles pass over an idler the higher ones travel a slightly longer path. This causes gaps to open in the microstructure, allowing small particles to percolate downwards. It also

generates a modest shear between the belt and the free surface. The combination of these induce a slow but relentless segregation. By 300 m the upper region of the belt material has become devoid of fines. Near the belt, large particles also migrate slowly upwards. By 1,350 m there is almost complete separation, with all the small particles adjacent to the belt and the large ones above.

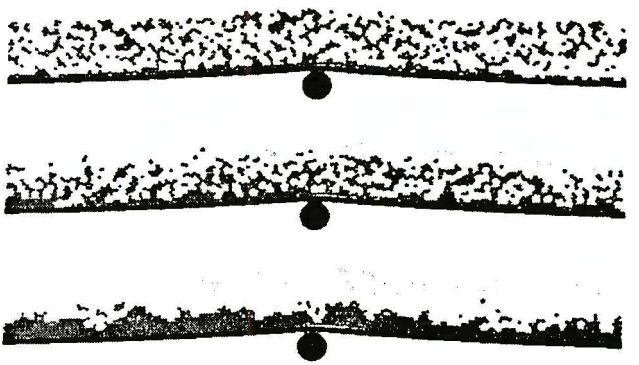

Figure 18. *Segregation on a conveyor belt, a) 6 m, b) 600 m and c) 4,050 m*

Simulations were performed for a range of size ratios D, and ratios of the total mass of large particles to small ones M. The segregation state can be measured by calculating local averages of particle diameter at a range of locations and characterising the resulting distribution by its coefficient of variation (section 3.2). There are two mechanisms of segregation. The small particles percolate relatively quickly down through the microstructure of large particles. This leads to a state (similar to Figure 18b) where a layer of large particles devoid of fines sits on top of a saturated layer of fines containing some large particles. The segregation rate is essentially constant with fluctuations superimposed. The second mechanism involves the fines pushing the remaining large particles up to the large particle region above. The segregation rate for this process is also relatively constant but is between 2 to 4 times slower. Eventually, this leads to a fully segregated state. It seems to be much faster for small particles to descend than it is for large ones to rise.

The fluctuations in the segregation rates have two main modes with periods around 4 s and 65-85 s. These are large compared to the fundamental period of 1 s (given by the time between idler encounters) and indicate that the flow is quite complex with processes occurring on a number of time scales. Surprisingly, these periods are relatively independent of both D and M. For small amounts of fines the amplitude of these cycles is relatively large. Increasing the amount of fines progressively smooths these cycles and leads to a more steady segregation process. The interface between the large particle region and the mixed region below is not parallel to the belt surface but appears to develop travelling waves which appear to be connected to the fluctuations observed in the segregation. The overall segregation rates increase approximately linearly with both D and M. This is easily understood

because smaller particles can fall through smaller gaps that occur more frequently and therefore lead to higher percolation rates. The larger M becomes, the smaller is the number of small particles that are competing to fall through these gaps, again leading to higher segregation rates.

9. Commodity Sampling by Cutters

Bulk commodities are frequently sampled by passing a cutter consisting of a pair of parallel blades through a stream of material falling from a conveyor belt. It is essential that the sample accurately reflects the original material. A typical arrangement is shown in Figure 19. The conveyor speed is 3 m/s and the particle top size is $D = 2$ cm. The cutter has 2 cm thick blades, 60° angle tips and an aperture of 2D and passes through the ore stream at 0.6 m/s and at a 30° angle.

Figure 19. *a) Iron ore sampling from a conveyor belt, b) ore passing through the sample cutter*

A mass weighted score, effectively an average diameter, was calculated for each sample taken and normalised by the value expected for perfect sampling. Figure 20a shows the scores for 46 simulations (with the same cutter design) and different sets of particles generated from the same size distributions. The expected value is given by the line at 100. There are substantial variations in the score

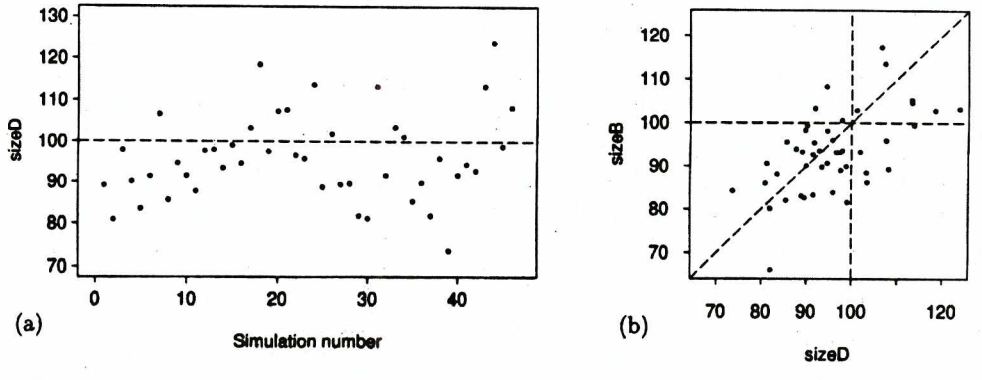

Figure 20. *a) Scores for 46 simulations, b) comparison of scores for two different blade shapes*

between simulations reflecting the wide differences produced by different sets of particles. The ensemble average of these (which reflects the long term sampling accuracy) shows a 9% under-sampling of the large particles (with 95% confidence limits of 8%). This means that this sample cutter is clearly biased.

Figure 20b compares the scores for this previous cutter to those for a matched set of 46 simulations using the same particle sets but with cutter possessing sharper symmetric edges. The matching of the simulations for the two cutters reduces the noise and makes the comparison statistically more accurate. This allows us to examine the effects of small changes in cutter design. For these two cutters, the points are clustered evenly around the 45º line indicating that there is no significant difference in the bias of the cutters. This is confirmed by a it *t*-test. In both cases there are more point below the 100% level indicating that they are both biased.

A wide range of cutter designs have been tested for a range of material properties and operating conditions. These are reported in [25] and show that many configurations that satisfy the requirements of Gy have demonstrated biases of 1 to 3% and low extraction ratios of 70-90% and that other cutters that do not satisfy these requirements have no detectable bias. Biases of the levels detected here have large economic significance for mining operations, particulalry for iron ore.

10. Mixing in a rotating tumbler

The location of the centroids of the two different materials is used to characterise the mixing in a rotating tumbler. The two materials exchange sides of the tumbler with a characteristic period T causing the centroid to behave as a decaying sinusoid. The exponential decay rate γ completely characterises the mixing rate.

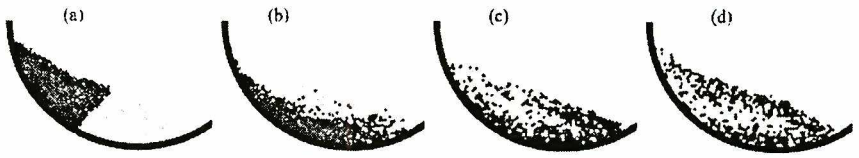

Figure 21. *Mixing for h=0.2 at a) 0.01, b) 0.5, c) 1.0 and d) 1.5 revolutions*

Figure 21 shows the mixing in a 30 cm tumbler rotating at 6 rpm filled to 0.2 of the tumbler height with two colours of circular particles of mean size 1.8 mm with a size variation of pm 2.4%. For this case we find $g = 0.7$ and $T = 0.61$. The closest available experimental results [26] give $\gamma \approx 2.5$ and $T \approx 0.23$. These were obtained for cubic salt particles with a mean size of 1.01 mm, a size range of ±20% and a tumbler rotation of 2.5 rpm. The real values of m and e are unknown. The simulation period T is about three times this value and the mixing rate is one quarter of the experimental value. Taking into account the effects of rotation rate and particle size there is still a discrepancy of a factor two.

Qualitatively, the simulated flow patterns are very similar to those of the experiments, but quantitatively, there is a sizable gap in the predicted mixing rates. The higher computed value of T gives us the needed insight. If all the particles away from the surface avalanching layer are moving with the tumbler in rigid body rotation (as is oberved in the experiments), then the period should theoretically be around 0.25. This is very close to the observed value. Our longer period and the visualisations of the simulated flow indicate that our flow has a slow but significant slumping deformation superimposed on the circulatory flow. The majority of the simulated material does not rotate rigidly. This leads to increase in T and decreases in gamma and demonstrates that the material shear strength is too low in the simulations.

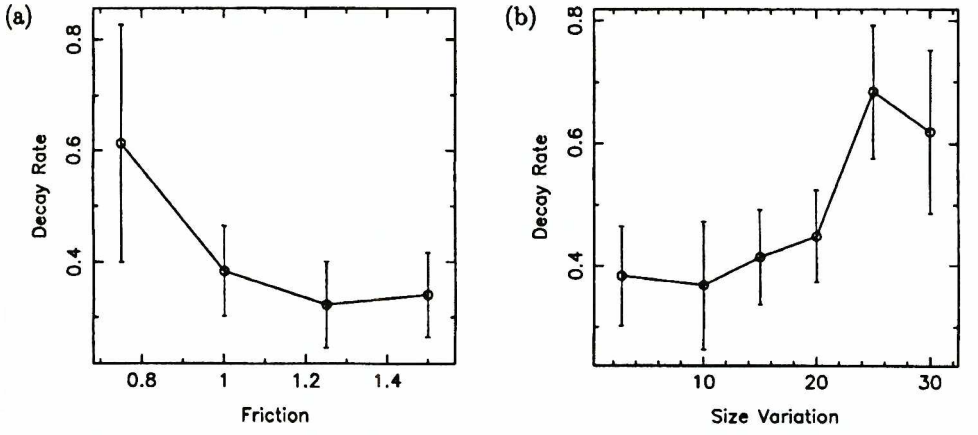

Figure 22. *Variation of mixing (decay) rate with a) friction and b) size distribution*

Figure 22 shows the behaviour of the mixing rate gamma with changes in the friction coefficient mu and the size distribution. Both γ and T are relatively constant for $\mu \geq 1$ and both increase for lower values. This is caused by the flow developing a partially slumping and partially circulating motion. This speeds the mixing but slows the centroid exchange and means that the slumping deformation is not due to friction effects. Similarly using the incorrect value for the coefficient of restitution can be ruled out.

The mixing is relatively insensitive to small variations in the particle size ranges, but for size variations of ±20% (or more) of the mean size, the mixing rate nearly doubles. The mixing period steadily declines as the size variation increases. Both these changes bring the simulation results closer to those of the experiments and reflect the increasing strength of the microstructure as the particle size distribution broadens. This increasing microstructure strength decreases the slumping deformation and makes the surface avalanching more energetic leading to better mixing. Changes in the size distribution can only increase the microstructure strength so far and even very large ranges are unable to reduce the difference in the mixing rate below a factor two. The dominant contribution to material strength in fact

comes from the particle shape. The material used in the experiments were relatively sharp edged cubic salt particles. These shape effects cannot be captured by the circular particles used in this simulation. More realistic particle shapes seem to be essential for DEM simulations to produce correct quantitative predictions for applications where stationary material shears and material strength is important.

Earlier we demonstrated that flows of circular particles in a centrifugal mill could be very accurately simulated using DEM. Here we show that applications with non-circular particles are poorly modelled by DEMs with circular particles. This underlines the crucial importance of including shape effects in our models. Non-circular shapes have a range of significant effects, including coupling the spin to the normal force. This alters the partitioning of energy and granular temperature between the linear and rotational modes and allows very rapid transference between modes. It also strongly changes the effective frictional properties of microstructure by eliminating the rolling mode of failure leaving only the sliding mode, thereby increasing the strength of the microstructure. It also leads to important dilation effects when the material actually does flow. This has particular implications for segregation and mixing. More detail of this application can be found in Cleary [17].

11. Mass flow in slot hoppers

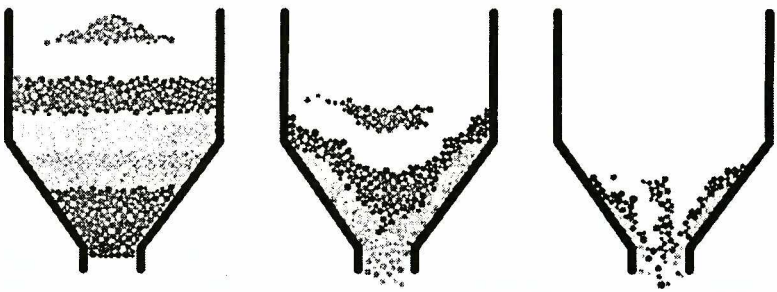

Figure 23. Mass flow from a slot hopper

Hoppers are common storage devices for granular materials. The dynamics of the filling and emptying are very important. Problems range from unwanted separation of components and flow blockage to structural failure. Figure 23 shows mass flow from a slot hopper. A rapidly moving central funnel dominates. This is surrounded by more slowly moving wedges to either side. Most of the material at the top flows out before the material on the sides. This occurs because the upper material is free to flow along the surface into the middle of the active funnel region, where it is travels down and out of the hopper. A range of useful predictions can be made for such flows. These include estimation of dynamic loads on the walls of hoppers. Slip-stick, cyclic stress variations and other problems can be identified.

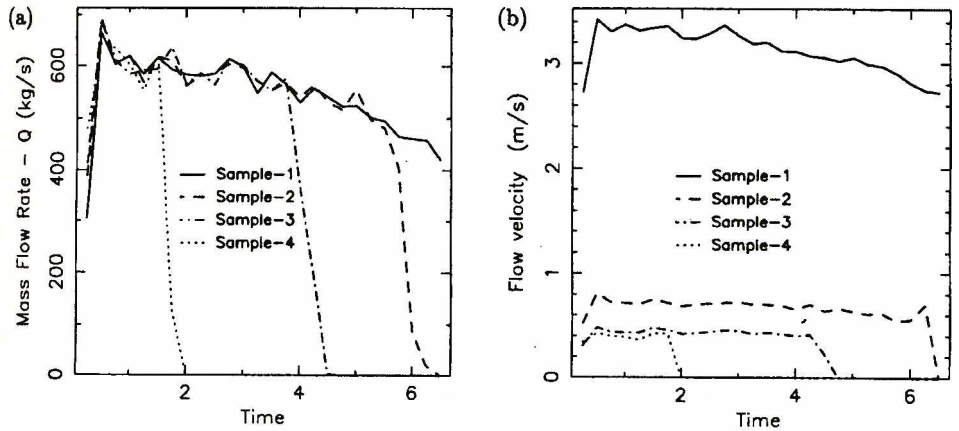

Figure 24. *For four different heights in the hopper: a) velocity flow rate and b) mass flow rate*

Sample line through the computational domain allows data to be gathered from inside the flow. Figure 24 shows the flow rates for a hopper similar to the one above, with sample lines were placed at: 1) in the opening, 2) halfway up the convergent section, 3) where the walls become vertical and 4) near the top. As the surface of the material falls below each sample line the flow rate through that sample lines obviously falls to zero. The mass flow rates are the same for each of the sample lines. This is reasonable since the material is relatively incompressible. The simulation predicts that the mass flow rate declines linearly from its initial peak of 600 to 450 kg/s as the head of pressure in the hopper declines. This is a substantially smaller decrease than would occur for a fluid because much of the weight of the solids is transmitted to the walls rather than to the opening. The particle velocities through each sample point are quite different. For the top two points (sample lines 3 and 4) where the walls of the hopper are parallel, the velocities are essentially the same at around 0.4 m/s. The flow rate half way down the convergent section has accelerated to about 0.7 m/s and the flow rate just below the opening is around 3 m/s. The velocities at the various heights do not vary much with time, except at the opening.

12. Choosing the model parameters

Choosing the model parameters so that they match those of real materials is a significant obstacle to DEM realising its potential as an accurate predictive tool. Even for simple contact force models, such as the linear spring-dashpot model used here, obtaining suitable values for the coefficients of friction μ and restitution ε is difficult. Direct measurement by carefully controlled experiment can provide estimates of ε but meaningful measurement of μ is made almost impossible for real industrial particles by the irregularity of the particle shape and its contribution to the resistance to flow. Our very strong feeling is that both particle-particle and particle-wall friction are best measured for collections of particles in calibration experiments. Numerical calibration experiments can then be used to determine μ_w and μ_p by matching the experimental calibration test.

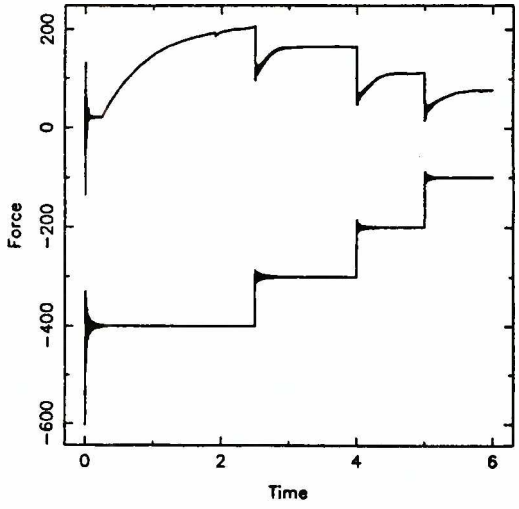

Figure 25. Shear stress as a function of applied normal stress in a numerical version of Jenike-Johansen style tester for wall particle friction

Figure 25 shows the result of a simulation of a Jenike-Johansen style shear tester on a sample of circular particles with diameters between 0.75 and 1.5 mm in a 40 mm wide chamber. A normal force N is applied to the top and the chamber is slide along a plate with a constant shear rate of 0.1 mm/s. The shear force required to maintain this motion is calculated. No consolidation is done before the measurements are taken. For this case the dynamic surface friction coefficient was $\mu = 0.75$ and $\varepsilon = 0.5$. The applied downward normal force is the lower of the two curves and begins at 400 N and is stepped down by increments of 100 N to examine the response of the material. The shear force is the upper curve. For both curves there are some short duration, very high frequency oscillations due to the response times of the springs in the contact force model. These decrease as the spring constant is increased and are typical of those found in all DEM simulations. This shows the importance of the DEM formulation being robust to numerical vibration.

After neglecting the oscillations, the shear force starts at a low level and then increases as the particles pack against the leading wall of the chamber and re-arrange their microstructure so that they are able to transmit force to their neighbours. The rate of shear force increase declines as progressively more of the particles become locked and transmit force. The asymptotic limit is the maximum amount of force that the now fully locked microstructure of particles can sustain. When the normal force is decreased, many of the contacts in the microstructure unload and the shear force decreases to well below its new asymptotic limit. The particles then re-arrange and the shear force rise back to this level. This pattern is continued for the subsequent decreases in normal force. The time taken to reach the

shear force limit is much smaller for the cases where the normal force is decreases because most of the particle re-arrangement (consolidation) has occured during the first loading phase and the relaxation during the decrease in load is small. It is important to note that in all cases the actual amount of movement involved in these re-arrangements is very small and barely perceptible. Movement by very small fractions of a particle diameter can have significant effects on the force networks that distribute the load within the microstructure and determine the shear force.

The effective wall-particle friction nu can be defined as the ratio of the shear force to the normal force. For the four load states, we find $\nu = 0.51, 0.54, 0.73, 0.78$ indicating that ν is a function of the load and for the higher load is much lower than the particle friction of 0.75. As the load decreases ν approaches this value. These variations arise from the particle microstructure which is in turn determined by the size and shape distribution. This type of test is therefore a very sensitive one that should allow good calibration of the DEM models.

13. Conclusion

DEM modelling is reaching a stage of development where significant industrial applications can be simulated reasonably well, provided that unrealistic assumptions are not made. A broad range of such applications have been simulated and are analysed in this paper. In two cases experimental data is available to validate the results. For centrifugal mills, where the particles were near spherical, the simulations using circular particles predicted the flow very well. For a slowly rotating cylinder filled with salt cubes, the DEM using circular particles produced poor results. This highlights the importance of particle shape and suggests that good predictions can be made if the shapes are characterised adequately.

For each application, relevant predictions were made including: wear rates and distributions, dynamic loads on boundaries, collisional force distributions, mass and velocity flow rates through arbitrary parts of the flow, mixing and segregation rates, power consumption, forces and torques. In each case, the predictions are qualitatively similar to the anecdotal data available to us. This demonstrates one of the greatest problems slowing the development of DEM simulation, which is obtaining sufficiently detailed and reliable experimental data with which to compare.

Another significant issue is the enormous difficulty involved in characterising real granular materials (size, density, shape, aspect ratio distributions, friction, resititution, hardness, abrasion characteristics) and measuring them. No matter how good the DEM tool itself may become, without good input data to drive it and without good experimental data to validate it, the opportunities to use its predictive capabilities will be limited and will produce erratic results.

Acknowledgements

Geoff Robinson's efforts in bringing the cutter sampling application to my attention and working with me on this problem over the last few years are gratefully acknowledged.

References

[1] Campbell C. S., 1990, *Rapid Granular Flows*, Annual Rev. Fluid Mech., **22**, 57-92

[2] Barker G. C., 1994, *Computer simulations of granular materials*, in: Granular Matter: An interdisciplinary approach, Ed. Anita Mehta, Springer-Verlag, NY

[3] Walton O. R., 1994, *Numerical simulation of inelastic frictional particle-particle interaction*, Chapter 25 of Particulate two-phase flow, ed M. C. Roco, 884 - 911

[4] Cleary P. W., Campbell C. S., 1993, *Self-lubrication for long run-out landslides: Examination by computer simulation*, J. Geophys. Res., 98, B12, pp. 21,911-21,924

[5] Campbell C. S., Cleary P. W., Hopkins M. A., 1995, *Large scale landslide simulations: Global deformation, velocities and basal friction*, J. Geophys. Res.

[6] Hopkins M. A., Hibler W. D., Flato G. M., 1991, *On the numerical simulation of the sea ice ridging process*, J. Geophys. Research

[7] Mishra B. K., Rajamani R. J., *The discrete element method for the simulation of ball mills*, App. Math. Modelling, 1992, 16, pp. 598-604

[8] Mishra B. K., Rajamani R. K., *Simulation of charge motion in ball mills*, Part 1: experimental verifications, Int. J. Mineral Processing, 1994, 40, 171-186

[9] Rajamani R. K., Mishra B. K., *Dynamics of ball and rock charge in sag mills*, Proc. SAG 1996, 1996, Department of Mining and Mineral Process Engineering, University of British Columbia

[10] Holst J. M., Rotter J. M., Ooi J. Y., Rong G. H., 1997, *Discrete particle and continuum modelling of particulate solids in silos: SILO FILLING*, Research report R97-007, Department of Civil and Environmental Engineering, University of Edinburgh, Edinburgh, EH9 3JN, UK

[11] Cleary P. W., 1993, *Modelling granular flows with complex boundary geometries*, Proc. 6th International Computational Techniques and Applications Conference, Eds. Stewart, D., Gardener, H., and Singleton, D., pp 148-155

[12] Cleary P. W., 1994, *Modelling industrial granular flows*, Proc. 1st Australian Engineering Mathematics Conference, pp. 169-177, Melbourne, 11-13th July, Eds. A. K. Easton and J. M. Steiner

[13] Cleary P. W., and Barton N. G., 1996, *Use of particle methods to design mineral processing equipment*, in Zeitschrift fur Angewandte Mathematik und Mechanik, 76, Supplement 4, Eds. E. Kreuzer and O. Mahrenholtz, Akademie Verlag, Berlin, 253-256

[14] Ansley and Kohn, *Filtering and smoothing in state space models with partially diffuse initial conditions*, J. Time Series Analysis, 11, 1990, pp 275-294

[15] Cleary P. W., 1996, *Discrete element modelling industrial granular flows*, Proc. 2nd Australian Engineering Mathematics Conference, pp. 301-308, Eds. W. Y., Yuen, Broadbridge, P., and Steiner, J. M., Institute of Engineers, Australia. Sydney, 15-17th July

[16] Cleary P. W., 1997, *Industrial particle flow modelling: Discrete element methods and their applications*, Proc. Chemeca 97, paper PT1a on CD Rom, reprinted in Chemeca97 Particle Technology Workshop, Ed. C. Davies, 1-12, Rotorua NZ

[17] Cleary P. W., Metcalfe G., and Liffman K., 1998, *How well do discrete element granular flow models capture the essentials of mixing and segregation processe?*, to appear: Applied Mathematical Modelling

[18] Schafer J., Dippel S., Wolf D. E., 1996, *Force schemes in simulation of granular material*, J. de Physique I.

[19] Hopkins M. A., 1987, *Particle Simulations*: Volume 1, Report No 87-7, Clarkson University, Potsdam, NY, USA

[20] Finnie I., 1960, *Erosion of surfaces by solid particles*, Wear, 3, 87 - 103

[21] Finnie I., 1972, *Some observations on the erosion of ductile metals*, Wear, 19, 81 - 90

[22] Hoyer, D.I., 1984, Particle trajectories and charge shapes in centrifugal mills, Proc. Int. Conf. on recent advances in mineral sciences and technology, MINTEK, South Africa, pp. 401-409

[23] Cleary P. W., 1998, *The filling of dragline buckets, to appear:* Mathematical Engineering in Industry

[24] Liffman K., Metcalfe G., Cleary P. W., 1997, *Particle Segregation and Convective Transport Due to Horizontal Shaking*, Phys. Rev. Lett., 79, 4574-4576

[25] Robinson G. K., and Cleary P. W., 1998, T*he conditions for sampling to be unbiased - Using Granular Flow Modelling to provide insight*, CSIRO Division of Mathematical and Information Sciences, Technical Report CMIS 98/70

[26] Metcalfe G., Shinbrot T., McCarthy J. J., Ottino J. M., 1995, *Avalanche mixing of granular solids*, Nature, 374 39-41